Influence of single-nanoparticle electrochromic dynamics on the durability and speed of smart windows

R. Colby Evans[a], Austin Ellingworth[b], Christina J. Cashen[a], Christopher R. Weinberger[c,d], and Justin B. Sambur[a,d,1]

[a]Department of Chemistry, Colorado State University, Fort Collins, CO 80523; [b]Department of Statistics, Winona State University, Winona, MN 55987; [c]Department of Mechanical Engineering, Colorado State University, Fort Collins, CO 80523; and [d]School of Advanced Materials Discovery, Colorado State University, Fort Collins, CO 80523

Edited by Catherine J. Murphy, University of Illinois at Urbana–Champaign, Urbana, IL, and approved May 7, 2019 (received for review January 4, 2019)

Nanomaterials have tremendous potential to increase electrochromic smart window efficiency, speed, and durability. However, nanoparticles vary in size, shape, and surface defects, and it is unknown how nanoparticle heterogeneity contributes to particle-dependent electrochromic properties. Here, we use single-nanoparticle-level electro-optical imaging to measure structure–function relationships in electrochromic tungsten oxide nanorods. Single nanorods exhibit a particle-dependent waiting time for tinting (from 100 ms to 10 s) due to Li-ion insertion at optically inactive surface sites. Longer nanorods tint darker than shorter nanorods and exhibit a Li-ion gradient that increases from the nanorod ends to the middle. The particle-dependent ion-insertion kinetics contribute to variable tinting rates and magnitudes across large-area smart windows. Next, we quantified how particle–particle interactions impact tinting dynamics and reversibility as the nanorod building blocks are assembled into a thin film. Interestingly, single particles tint 4 times faster and cycle 20 times more reversibly than thin films made of the same particles. These findings allow us to propose a nanostructured electrode architecture that optimizes optical modulation rates and reversibility across large-area smart windows.

single-particle electro-optical imaging | tungsten oxide | single-particle electrochromism | ion-insertion kinetics

The "smart" glass industry is developing window tinting technologies that modulate the amount of visible and infrared radiation transmitted into aircraft, automobiles, and buildings to increase occupant comfort and decrease energy consumption (1–4). Smart windows are typically based on electrochromic tungsten oxide films (5–10), whose tunable optical properties stem from the electrochemical ion-insertion/-extraction reaction in Eq. **1**. Applying a cathodic potential induces tinting, or coloration, where electrons (e^-) and cations (M^+) (such as H^+ or Li^+) are injected into the transparent WO_3 material, forming a deep blue M_xWO_3 compound. Applying an anodic potential induces bleaching, where electrons and cations are extracted from the colored M_xWO_3 compound, reforming the transparent WO_3 material. State-of-the-art electrochromic smart windows switch from transparent to 90% fully tinted states in 7 to 12 min (11). Since smart windows consume the most energy during the tinting process (12), there is a strong interest in increasing the coloration efficiency (color change per unit charge inserted into the electrochromic material) to decrease the energy required for window tinting:

$$WO_3 + xM^+ + xe^- \rightleftarrows M_xWO_3. \quad [1]$$

Electrochromic nanoparticles have unique properties that potentially enable faster tinting rates and longer lifetimes compared with thin films (13, 14). First, nanostructured electrodes enable more ion-insertion reactions per geometric area than planar electrodes. Since more color centers are produced near the solid/electrolyte interface, cations traverse less distance during coloration/bleaching cycles; both effects potentially improve coloration/bleaching kinetics and electrochemical reversibility. Second, nanoparticles exhibit size-dependent pseudocapacitive electrochemical properties (15). Pseudocapacitive electrochromic nanoparticles increase tinting rates (16–19) due to rapid surface ion-insertion reactions rather than a slow bulk ion-insertion process.

Despite the potential advantages of electrochromic nanoparticles for smart window applications, it is unknown how nanoparticle heterogeneity contributes to particle-dependent coloration efficiency, coloration/bleaching kinetics, and optical-density (OD) magnitude. Particle-dependent electrochromic behavior across square meter-sized windows contributes to spatially nonuniform tinting. In situ optical-based (20–22), electron-based (23), and X-ray–based (24, 25) microscopy techniques have been used to image ion-insertion kinetics and structural transitions in electrochromic metal oxide films and single particles, but it is challenging for the electron and X-ray approaches to study electrochromic properties under device-relevant conditions such as ambient pressure, temperature, and radiation doses.

In this work, we use a single-particle-level optical imaging approach to determine structure–function relationships in

Significance

"Smart" windows reduce electricity consumption associated with cooling buildings by blocking thermal radiation from the sun, or heat, from entering buildings. However, state-of-the-art smart windows require 7 to 12 min to modulate between transparent and dark states. Nanomaterials have the potential to tint faster and more efficiently than bulk materials, but it is unclear how structural differences among nanoparticles influences their optical modulation behavior. Here, we identify champion particles that tint the fastest and block the most radiation by watching single nanoparticles in a model smart window device. In addition, we observed that interfaces between particles contribute to long-term device degradation. These findings allow us to propose a new nanoparticle-based window design that optimizes tinting rates and promotes long-term stability.

Author contributions: R.C.E. and J.B.S. designed research; R.C.E. performed research; R.C.E., A.E., C.J.C., C.R.W., and J.B.S. analyzed data; and R.C.E., C.R.W., and J.B.S. wrote the paper.

Conflict of interest statement: R.C.E. and J.B.S. filed a provisional patent based on the findings in this study.

This article is a PNAS Direct Submission.

Data deposition: The raw image files and codes to analyze the data have been deposited in the Mountain Scholar repository, https://hdl.handle.net/10217/195014

[1]To whom correspondence may be addressed. Email: jsambur@colostate.edu.

This article contains supporting information online at www.pnas.org/lookup/suppl/doi:10.1073/pnas.1822007116/-/DCSupplemental.

Published online June 3, 2019.

pseudocapacitive hexagonal WO_3 nanorods and quantify the impact of particle–particle interactions on electrochromic dynamics. Our measurements revealed a particle-dependent waiting time for coloration due to Li-ion insertion at optically inactive surface sites. Longer nanorods tend to tint darker because they store more Li-ion color centers at surface step sites, and an internal electric field drives Li-ion transport from the nanorod ends toward the middle. The particle-dependent waiting time, coloration rates, and magnitudes contribute to unwanted spatial and temporal tinting performance across large-area electrochromic windows. In addition, we discovered that particle–particle interfaces contribute to long-term irreversible tinting in nanoparticle-based electrochromic smart windows.

Results and Discussion

Single-Particle Electrochromism Imaging Approach. Fig. 1 shows the experimental methodology for imaging Li-ion insertion/extraction processes in single hexagonal WO_3 nanorods (h-WO_3 NRs) (average length = 1.02 ± 0.54 μm and width = 0.10 ± 0.04 μm; *SI Appendix*, Fig. S1). Each nanorod is a single crystal with well-defined {1000} surface facet orientations for the sidewalls (*SI Appendix*, Fig. S1*B*). We assembled a h-WO_3 nanorod-coated tin-doped indium oxide working electrode (h-WO_3 NR/ITO) into a three-electrode microfluidic electrochemical cell and mounted it on the stage of an inverted optical microscope (Fig. 1*A*). A 940-nm light-emitting diode (LED) illuminates the sample, and an electron-multiplying charge-coupled device camera acquires images that are synchronized with the current-time response of the electrochemical cell (Fig. 1*B*). The WO_3 nanorods appear as dark objects against a bright background in optical transmission images because the particles absorb and scatter incident light. Ex situ scanning electron microscopy (SEM) imaging confirms that the dark objects in optical images are either isolated or clustered h-WO_3 NRs (Fig. 1 *C* and *D*).

To induce the coloration and bleaching process according to Eq. **1**, cathodic and anodic voltage pulses were applied to the h-WO_3 NR/ITO electrode in a propylene carbonate electrolyte containing 1.0 M $LiClO_4$ (Fig. 1*E*). We calculate the particle thickness (d) corrected change in OD, $\Delta OD(t)_d = OD(t)_d - OD(0)_d = -log_{10}\left(\frac{I(t)}{I_0(t)}\right) + log_{10}\left(\frac{I(0)}{I_0(0)}\right)$, where I_0 and I are the transmitted light intensities through the ITO substrate and WO_3 particle, respectively (indicated by dashed and solid red lines in Fig. 1 *B*–*D*; also see *Methods*). Fig. 1*F* shows a representative $\Delta OD(t)_d$ trajectory from the single nanoparticle in Fig. 1*D*, where the OD expectedly increases and decreases during cathodic and anodic voltage pulses. The widefield imaging approach measures hundreds of nanoparticles in a single experiment. We observed that 9% (9 of 102) of single particles showed no optical modulation and 6% (6 of 102) of single particles showed anomalous tinting behavior during cathodic polarization cycles (*SI Appendix*, Fig. S2). The potential significance of the inactive and anomalous particles will be discussed below.

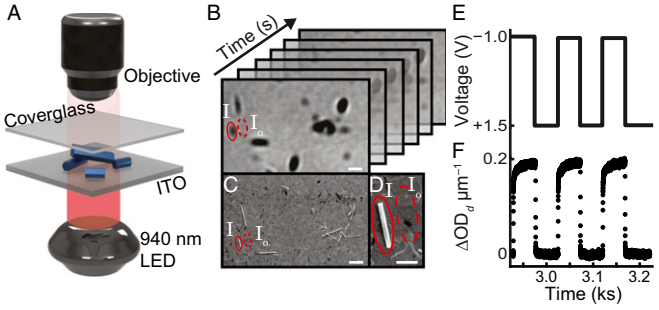

Fig. 1. Single-nanoparticle electrochromism imaging approach. (*A*) Electrochemical setup for widefield optical imaging of single-nanoparticle electrochromism. Pt counter and Ag/AgCl reference electrodes are not shown for clarity. (*B*) Optical transmission image stack during a cathodic polarization pulse. The solid and dashed red lines indicate equivalent-sized regions to calculate the light intensity transmitted through a WO_3 nanoparticle (I) and ITO substrate (I_0), respectively. (Scale bar, 1 μm.) (*C*) SEM image of the sample region in *B*. (Scale bar, 1 μm.) (*D*) Zoom-in of the single nanorod indicated by the solid red lines in *B* and *C*. (Scale bar, 500 nm.) (*E* and *F*) Potential versus time waveform applied to the h-WO_3 NR/ITO electrode (*E*) and the thickness-corrected $\Delta OD(t)_d$ versus time trajectory from the particle (*F*) in *D*.

Modeling Coloration and Bleaching Dynamics in Single h-WO_3 Nanorods. Fig. 2 shows representative $\Delta OD(t)_d$ trajectories for three isolated nanorods with similar widths (0.11, 0.16, and 0.10 μm) and different lengths (1.64, 0.52, and 0.67 μm). The $\Delta OD(t)_d$ trajectories exhibit three distinct features: (*i*) a particle-dependent waiting time for a change in OD (t_{wait}) (Fig. 2 *C*, *F*, and *I*), (*ii*) an abrupt OD burst at short times, and (*iii*) a steady OD increase at long times (Fig. 2 *B*, *E*, and *H*). To explain the particle-dependent waiting time, we consider that h-WO_3 has three Li-ion binding sites: hexagonal windows (HWs), square windows (SWs), and trigonal cavities (TCs) (*SI Appendix*, Fig. S3) (26–29). Balaji et al. showed that Li ions fill TC sites first, but only HW and SW sites contribute to coloration in macroporous hexagonal WO_3 films (28), in agreement with electronic structure calculations (27). For these h-WO_3 NRs, ensemble-level electro-optical, electrochemical current, and Raman spectroscopy measurements show that Li ions and electrons are injected into the WO_3 particles from t = 0 to $t = t_{wait}$ even though there is no OD change (*SI Appendix*, Figs. S4 and S5). Thus, we attribute the waiting time to Li-ion insertion at optically inactive TC sites.

To explain the OD burst behavior, we analyzed cyclic voltammetry data and concluded that these h-WO_3 nanorods exhibit pseudocapacitive electrochemical behavior (*SI Appendix*, Fig. S5*B*) (30). Pseudocapacitance is a faradaic capacitive charging process that is associated with rapid charge transfer reactions at or near the electrode surface (16). The OD burst behavior can be attributed to Li-ion insertion at optically active HW and SW surface sites because we observed that $\Delta OD(t)_d$ scales exponentially with t, consistent with a capacitive surface charging process. Intercalation pseudocapacitance throughout the nanorod bulk is not expected in these h-WO_3 nanorods because bulk pseudocapacitance requires a unique crystalline network (31). The slow OD rise behavior can be attributed to a diffusion-limited Li-ion insertion process at bulk HW and SW sites because we observed that $\Delta OD(t)_d$ scales with $t^{1/2}$ at long times, in agreement with the Cottrell equation (22). While we do not image directly Li-ion insertion at bulk versus surface sites, we distinguish the rapid surface Li-ion insertion reaction (i.e., pseudocapacitance) from the slow bulk Li-ion insertion process, respectively, in agreement with the literature (17, 18, 32–35).

To quantitatively analyze the $\Delta OD(t)_d$ trajectories of 102 individual h-WO_3 NRs, we developed a time-dependent electrochromism model that accounts for (*i*) t_{wait}, (*ii*) the pseudocapacitive OD burst, and (*iii*) the slow OD rise (see *Methods*). In this model, Li-ion insertion at reduced W^{5+} sites are responsible for coloration as we observe no W^{4+} species in X-ray photoelectron spectroscopy measurements (*SI Appendix*, Fig. S6) (36). Fitting Eq. **2** in *Methods* to the $\Delta OD(t)_d$ data (see solid red lines in Fig. 2 *B*, *E*, and *H*) yields t_{wait}, a rate constant for the surface charge transfer reaction (k_{surf}), and the total charge inserted into optically active bulk and surface HW and SW sites (Q_{bulk}^{active} and Q_{surf}^{active}). In addition, we extract smart window performance metrics such as the particle thickness-corrected maximum change in OD (ΔOD_d^{max}), the time required to reach 90% of ΔOD_d^{max} (t_{90}^{color}), and the time required to decay from ΔOD_d^{max} by 90% (t_{90}^{bleach}).

Effect of Particle Size and Surface Structure on OD Magnitude and Dynamics. Fig. 3*A* shows a positive Pearson correlation coefficient between ΔOD_d^{max} and nanorod length; on average, longer nanorods tint darker than shorter nanorods. However, particles

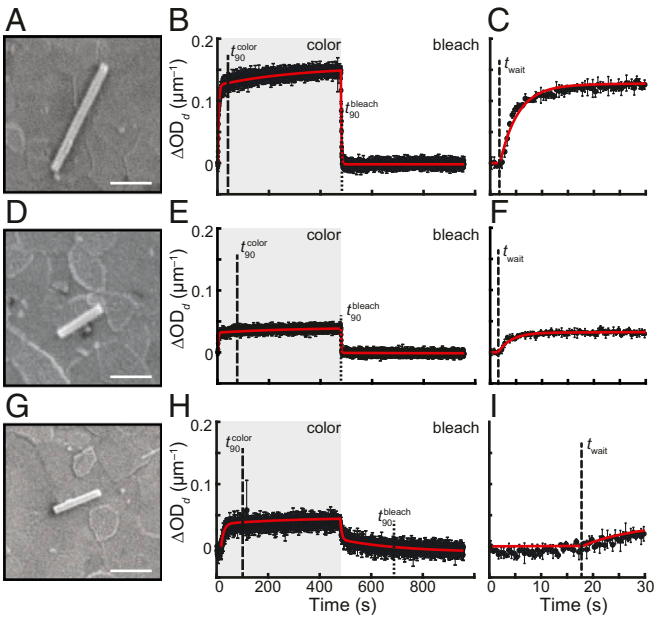

Fig. 2. Quantitative analysis of single-nanoparticle OD trajectories. (*A*) SEM image of a single WO_3 nanorod (length = 1.64 μm, width = 0.11 μm). (*B*) $\Delta OD(t)_d$ trajectory of the same nanorod in *A*. The $\Delta OD(t)_d$ data points and error bars represent the mean and SD of three consecutive cathodic (−1.0 V vs. Ag/AgCl) and anodic (+1.5 V vs. Ag/AgCl) potential cycles. The dashed vertical lines represent t_{90}^{color} (67.78 s) and t_{90}^{bleach} (4.33 s). The solid red line represents the fit to the data using Eq. **2** in *Methods*. (*C*) $\Delta OD(t)_d$ trajectory in *B* from $t = 0$ to 30 s, showing $t_{wait} = 1.78$ s. (*D–F*) Same data as *A–C*, but for a shorter WO_3 nanorod (length = 0.52 μm, width = 0.16 μm) with longer t_{90}^{color} (115.53 s), t_{90}^{bleach} (3.33 s), and slightly longer t_{wait} (2.78 s). (*G–I*) Same data as *A–C*, but for a shorter WO_3 nanorod (length = 0.67 μm, width = 0.10 μm) with longer t_{90}^{color} (96.78 s), t_{90}^{bleach} (209.33 s), and much longer t_{wait} (18.03 s). (Scale bars, 500 nm.)

with identical lengths can exhibit an order of magnitude difference in ΔOD_d^{max} under identical experimental conditions. Our trajectory analysis revealed that longer nanorods store more surface charge per geometric area (Fig. 3*B*) and more bulk charge per volume than shorter nanorods (Fig. 3*C*). These trends are hidden in ensemble-level electro-optical measurements and unexpected because the number density of Li-ion binding sites does not scale with surface area and volume in perfect crystals.

To understand the bulk and surface charge storage trends with nanorod length (Fig. 3 *B* and *C*), we analyzed $\Delta OD(t)$ along the length of single nanorods (Fig. 3*D*). The $\Delta OD(t)$ kinetics are independent of position along the nanorod (Fig. 3*E*), but the maximum OD increases from the nanorod ends toward its middle (Fig. 3*F*). The OD trend in Fig. 3*F* indicates that more (Li^+-W^{5+}) color centers accumulate in the middle of the nanorod than at its ends even though there are no observable structural gradients along the nanorod in SEM images (Fig. 3*D*). Interestingly, the slope of the color center gradient is larger for nanorods with larger ΔOD^{max} values (Fig. 3*G*). One explanation for the (Li^+-W^{5+}) color center gradient is a surface step-edge gradient that propagates from the nanorod middle to the ends, as evidenced by transmission electron microscopy imaging of separate nanorods from the same sample (*SI Appendix*, Fig. S7). Highly stepped surfaces have more Li-ion insertion sites than smooth surfaces and therefore more optically active surface sites per geometric area than a perfect crystal (*SI Appendix*, Fig. S8 *A* and *B*). Since the nanorods grow outward from a preformed core (37, 38) and the growth rate of different crystal planes varies (37), then a defect gradient could develop along the nanorod side facets (39) with the highest defect density at the nanorod center and the lowest defect density at the ends (40). Another possibility for the trend in Fig. 3*C* is that electric fields at step edges facilitate Li-ion transport from the nanorod ends toward the middle along the large hexagonal channels of *h*-WO_3 nanorods (*SI Appendix*, Fig. S8*C*) (41–43).

Having determined the correlation between nanorod structure and OD magnitude, we then explored optical modulation kinetics at the single-nanorod level. Interestingly, we observed no strong correlations between OD kinetic parameters (e.g., t_{90}^{color}, t_{90}^{bleach}, t_{wait}, and k_{surf}) and particle length, width, geometric surface area, or volume (*SI Appendix*, Figs. S9–S11). The fact that t_{90}^{color}, t_{90}^{bleach}, t_{wait}, and k_{surf} are not correlated with bulk structural properties implies that electrochromic kinetics are dominated by particle-dependent properties such as defect sites. The presence of impurity atoms and defects are unavoidable for nanomaterial samples that even share the same side facets [they also occur in bulk WO_3 (44)]. Our single-particle approach circumvents the issue of particle-to-particle heterogeneity, a challenge for conventional ensemble measurements that average differences among particles.

We expected to observe a correlation between t_{wait} and nanorod length because longer nanorods with more step edges would have more optically inactive TC sites that contribute to a longer t_{wait} (*SI Appendix*, Fig. S8*B*). However, the waiting time is independent of nanorod length (Fig. 4*A*) and other structural properties (*SI Appendix*, Fig. S10). We observed that optically active surface charge density is more strongly correlated with nanorod length than optically inactive charge density (Pearson correlation coefficient $\rho = 0.52 \pm 0.06$ in Fig. 3*B* versus $\rho = 0.14 \pm 0.07$ in *SI Appendix*, Fig. S10*D*). The optically active surface charge density is more strongly correlated with nanorod length than the inactive charge density presumably because (*i*)

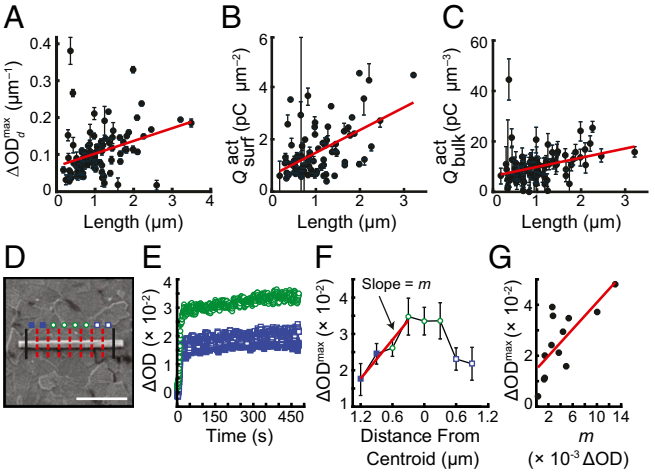

Fig. 3. Correlation between OD magnitude and nanorod structural properties. (*A*) The particle thickness-corrected change in OD (ΔOD_d^{max}) versus nanorod length (Pearson correlation coefficient $\rho = 0.34 \pm 0.06$; $n = 98$ particles). (*B* and *C*) Charge inserted into optically active surface sites per electrochemically active surface area of the nanorod Q_{surf}^{active} versus length ($\rho = 0.52 \pm 0.05$, $n = 83$ particles) (*B*) and bulk charge per unit volume Q_{bulk}^{active} versus length ($\rho = 0.33 \pm 0.07$, $n = 83$ particles) (*C*). The black circles in *A–C* represent data from individual nanorods and the solid red line is a linear fit to show the general trend. (*D*) SEM image of a single nanorod. The distance between all vertical black and red lines are 200 nm. The nanorod end segments beyond the vertical black lines were not analyzed. (Scale bar, 1 μm.) (*E*) Representative $\Delta OD(t)$ trajectories measured from the middle (hollow green circles) and end segments (hollow and solid blue squares) on the single nanorod in *D*. (*F*) ΔOD^{max} versus distance from nanorod centroid calculated from the trajectory analyses in *E*. The red line represents a linear fit to the segmented data. Error bars are the SD of ΔOD within the segment. (*G*) ΔOD^{max} of 13 single particles versus its slope parameter defined in *F*. The red line is a linear fit to show the general trend ($\rho = 0.73 \pm 0.31$).

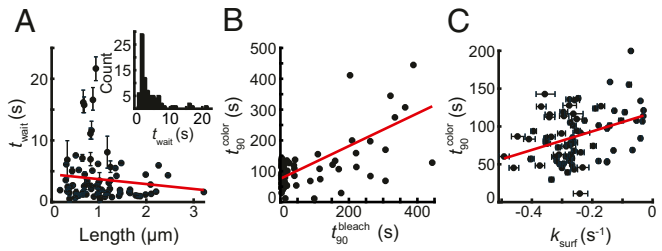

Fig. 4. Coloration and bleaching kinetics at the single particle-level. (*A*) Waiting time for optical modulation versus nanorod length ($\rho = -0.11 \pm 0.07$). *Inset* shows the distribution of waiting times. (*B*) Coloration versus bleaching kinetics; t_{90}^{color} versus t_{90}^{bleach} ($\rho = 0.65 \pm 0.04$). (*C*) t_{90}^{color} versus k_{surf} ($\rho = -0.38 \pm 0.06$). The black circles in *A*–*C* represent data from single nanorods and red line is a linear fit to show the general trend. Error bars in *A* and *C* are defined in *SI Appendix*, section 16.

the large hexagonal tunnels accommodate more Li ions than the small trigonal cavity tunnels (45) and (*ii*) Li-ion transport is more efficient in the large, open hexagonal tunnels than in the smaller trigonal tunnels (43). Regardless of the underlying reason why t_{wait} and optically inactive surface charge is independent of length, the large variation in waiting times, from 100 ms to 20 s (Fig. 4*A*, *Inset*), is significant because particles with longer waiting times decrease coloration efficiency; no OD change occurs even though charge is inserted into the nanorods.

A particle's maximum OD is not correlated with its coloration and bleaching kinetics; particles that tint faster do not necessarily tint darker (*SI Appendix*, Fig. S11). Instead, Fig. 4*B* shows that coloration and bleaching kinetics are strongly correlated (i.e., positive Pearson correlation coefficient), indicating that particles that color faster also bleach faster. The optical modulation times are extremely heterogeneous; some nanoparticles achieve 90% OD modulation in 12 s, whereas other nanoparticles require 275 s. The strongest predictor of fast coloration in these *h*-WO_3 NRs is fast pseudocapacitive charge-transfer kinetics (Fig. 4*C*). The trend in Fig. 4*C* suggests that Li-ion insertion at the WO_3/electrolyte interface, rather than Li-ion diffusion in the WO_3 interior, accounts for large heterogeneities in coloration/bleaching kinetics at the single-particle level, likely due to the particle-dependent stepped-surface structure (e.g., *SI Appendix*, Fig. S7).

While our approach does not measure electrochemical current at the single-nanoparticle level, this apparent experimental limitation does not restrict the conclusions regarding the structure function relationships of our study. Regardless of the electrochemical current flow into single particles, we still measured that longer nanorods tint darker than shorter nanorods and longer nanorods exhibit a color center gradient. These structure/property relationships hold regardless of the electrochemical current into the nanoparticles. Importantly, all of the above observations were made from single particles that are attached to the same ITO electrode, immersed in the same electrolyte, and located only microns apart.

Role of Particle–Particle Interfaces on Electrochromic Dynamics and Reversibility. To probe whether the electrochromic properties of nanoparticle building blocks are maintained in thin-film electrodes, we studied how electrochromic dynamics and reversibility scale with the number of particle–particle interactions as the building blocks are assembled into a thin-film electrode. To do so, we compared single particle $\Delta OD(t)$ trajectories to those measured from particle clusters containing two, three, four, or five *h*-WO_3 nanorods. In addition, we measured $\Delta OD(t)$ trajectories of large clusters (25 to 100 particles) and a thin-film electrode. For example, Fig. 5*A* shows an SEM image of a cluster containing three *h*-WO_3 nanorods and Fig. 5 *B* and *C* shows its normalized $\Delta OD(t)$ response (black trace) compared with the average trajectory of 98 isolated *h*-WO_3 nanorods (blue trace). *SI Appendix*, Fig. S12 shows representative SEM images and $\Delta OD(t)$ responses for all cluster sizes. The three-particle cluster showed similar $\Delta OD(t)$ dynamics compared with single particles (Fig. 5 *B* and *C*) and qualitatively reversible electrochromic behavior (Fig. 5*D*). For large nanoparticle clusters (Fig. 5 *E*–*H*) and the thin-film electrode (Fig. 5 *I*–*L*), the $\Delta OD(t)$ kinetics and reversibility deviate from the single particle building blocks.

To quantify the role of particle–particle interactions on tinting dynamics and reversibility, we extracted t_{90}^{color}, t_{90}^{bleach}, and the fraction of electrochromic cycles that do not return to the original transparent state for 298 clusters and 894 cycles (*SI Appendix*, section 15). Cluster size-dependent coloration magnitude was not analyzed because OD depends on cluster thickness and it was difficult to measure cluster thickness via SEM and atomic force microscopy imaging. Fig. 6*A* shows that t_{90}^{color} and t_{90}^{bleach} are independent of particle–particle interactions in the small cluster limit (two to five particles), but then both parameters increase for large clusters and the thin-film electrode. The electrochromic dynamics of small particle clusters are unaffected presumably because each particle within the cluster remains in contact with the ITO electrode and the liquid electrolyte. As the number of particle–particle interactions increases (i.e., for 25- to 100-particle clusters and the thin-film electrode), the optical modulation kinetics decrease because electrons and Li ions must traverse multiple particle–particle interfaces. On the other hand, an alternative possibility is that one anomalous single particle in one large nanoparticle cluster dominates the $OD(t)$ response because we observed that the $OD(t)$ kinetics of anomalous particles are strikingly similar to large clusters and the thin-film electrode (*SI Appendix*, Fig. S2). However, it remains unclear to what extent a single anomalous particle impacts the kinetics and reversibility of an entire cluster.

While tinting rates are independent of particle cluster size in the few particle regimes, the frequency of irreversible bleaching cycles increases monotonically with particle–particle interactions (Fig. 6*B*). In other words, large particle clusters remain tinted following an anodic polarization treatment. This persistent tinting effect has been attributed to ion trapping in WO_3 thin films (46). For these *h*-WO_3 nanorods, the irreversible bleaching effect onsets for two particle-sized clusters due to (Li-W^{5+}) color

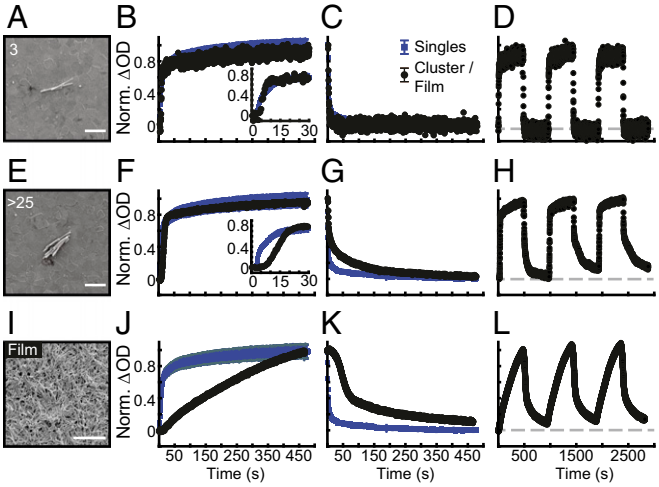

Fig. 5. Electrochromic dynamics and reversibility of nanorod clusters and thin films. (*A*) SEM image of a particle cluster containing three nanorods. (*B* and *C*) $\Delta OD(t)$ trajectory of the cluster in (*A*, black trace) compared with the average trajectory of 102 single nanorods (blue trace). (*D*) $\Delta OD(t)$ trajectory for the cluster in *A* during three consecutive color and bleaching cycles. The dashed horizontal line in *D* represents ΔOD at 0 s. *E*–*L* are the same as *A*–*D*, but for a large 25- to 100-particle cluster and a thin-film electrode, respectively. (Scale bars: *A* and *E*, 1 μm; *I*, 10 μm.)

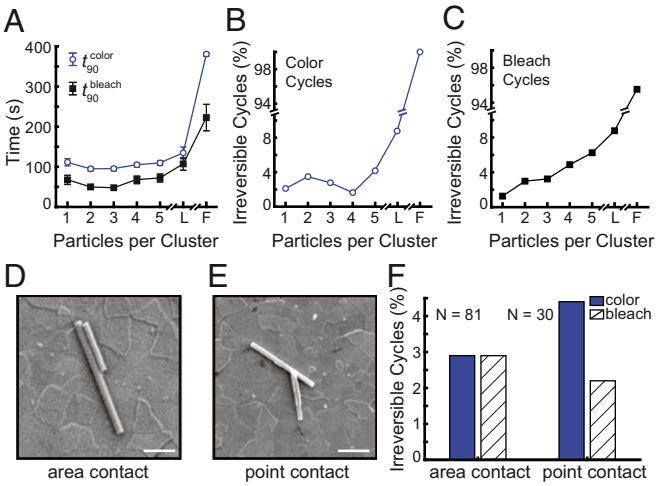

Fig. 6. Role of particle–particle interactions on electrochromic dynamics and reversibility. (*A*) t_{90}^{color} and t_{90}^{bleach} versus particle cluster size. F, nanorod thin film; L, large clusters (>25 particles). (*B* and *C*) Fraction of irreversible bleaching (*C*) and color (*B*) cycles versus particle cluster size. The total number of clusters analyzed for sizes 2, 3, 4, 5, and >25 were 134, 72, 41, 32, and 19, respectively. Error bars in *A*–*C* represent the standard error of the mean. (*D* and *E*) SEM image of a two-particle cluster with side-by-side (area contact) configuration and top-and-bottom (point contact) configuration. (Scale bars, 1 μm.) (*F*) Fraction of irreversible coloration and bleaching cycles for 81 side-by-side clusters (243 total cycles) and 30 top-and-bottom clusters (90 total cycles).

centers that remain trapped at the nanorod–nanorod interface. The interfacial trapping sites could be due to Li-ion insertion at W = O surface sites on neighboring particles (47), leading to a more stable LiO_x-type interaction (*SI Appendix*, Fig. S7*C*). While the exact trapping site is currently unknown, our results show that extrinsic ion-trapping sites are introduced at particle–particle interfaces; the trapping site is not intrinsic to the nanorod. On the other hand, electrochromic coloring reversibility is independent of particle–particle interactions in the single and few particle cluster regimes and then abruptly increases for large clusters and the thin-film electrode (Fig. 6*C*). This trend could be due to the trapped (Li-W^{5+}) color centers at particle–particle interfaces that decrease the number of available Li-ion binding sites in consecutive cycles.

To explore how interfacial contact area between nanorods influences electrochromic reversibility, we analyzed the electrochromic reversibility of two-particle clusters with area versus point contact configurations. Fig. 6*D* shows a representative SEM image of a two-particle cluster where the nanorods align in a side-by-side configuration. Fig. 6*E* shows a two-particle cluster in a top-and-bottom configuration where one nanorod lays on top of another particle. The side-by-side configuration has a larger particle–particle contact area than the top-and-bottom configuration (see additional examples in *SI Appendix*, Fig. S13). Two-particle clusters with side-by-side contacts exhibit less irreversible coloration and more irreversible bleaching behavior than clusters with point contacts (see blue bars versus patterned white bars in Fig. 6*F*). We attribute the increase in irreversible electrochromic behavior to the large interfacial contact area that introduces more extrinsic ion-trapping sites between two nanorods. The coloration reversibility difference between the different cluster configurations is likely due to differences in the electron injection pathway. The electron-injection pathway for the side-by-side configuration is similar to isolated nanorods; the ITO electrode contacts each nanorod in the cluster along the entire nanorod sidewall (Fig. 6*A*). The pathway for the top-and-bottom configuration occurs at the nanorod end points (either at the nanorod–nanorod interface or the ITO–nanorod interface). It is possible that electron-injection efficiency at the nanorod–nanorod interface decreases with cycle number due to the accumulation of trapped ions at the solid–solid interface.

Two-particle clusters with large-area contacts modulate from the bleached state to the colored state more reversibly than from the colored state to the bleached state (Fig. 6*F*). We observed the opposite effect for two-particle clusters with point contacts; the cluster modulates from the colored state to the bleached state more reversibly than from the bleached state to the colored state. The exact origin of these trends is currently unknown since the ion-trapping sites and mechanisms are likely different in the coloring and bleaching processes (48). It is possible that the different particle–ITO and particle–particle contacts for each cluster configuration influence the coloration and bleaching reversibility differently.

In summary, our measurements reveal underlying electro-optical processes that contribute to performance heterogeneity across large-area electrochromic nanoparticle films. First, the particle-dependent waiting time for coloration contributes to a delay time for window tinting and diminishes electrochromic coloration efficiency. The overall performance effect is that the window tints gradually in space and time as particles stochastically switch one-by-one from the transparent to colored state. Second, individual nanoparticle building blocks can tint up to 400% faster than a nanoparticle film assembled from the same building blocks. Finally, ion-trapping sites are introduced at particle–particle interfaces that cause long-term optical performance degradation. We propose to overcome these challenges using a mesoporous thin-film architecture, where fast-switching electrochromic nanoparticles are deposited onto a high surface area transparent conductor (*SI Appendix*, Fig. S14). This strategy would enable total light absorption with single layers of WO_3 particles, thereby avoiding deleterious particle–particle interactions. Our single particle electrochromism imaging approach can be generally applied to transition metal oxides (49, 50), graphite (51, 52) and $Ni(OH)_2$ battery materials (53) whose optical properties change during ion insertion. Single particle electro-optical imaging of ion-insertion/-extraction processes can guide applied research related to batteries, fuel cells, electrochemical capacitors, and sensors.

Methods

Materials Synthesis and Characterization. Hexagonal WO_3 nanorods were synthesized via a hydrothermal reaction following Wang et al. (37). Ensemble-level structural characterization (*SI Appendix*, section 1) shows that these nanorods have a hexagonal crystal structure, and we assume that the particles have a square rectangle morphology (average length = 1.02 ± 0.54 μm and width = 0.10 ± 0.04 μm; n = 258 particles), in agreement with Wang et al. (37).

Single-Nanoparticle Electrochromism Measurements and Image Analysis. All electrochemical measurements were performed in 1 M $LiClO_4$ in propylene carbonate in a three-electrode microfluidic electrochemical cell using a Pt wire counter electrode and a Ag/AgCl reference electrode. The electrochemical cell was mounted on the stage of an inverted optical microscope (Olympus IX73; Fig. 1*A*). Detailed flow cell preparation and electro-optical imaging procedures are provided in *SI Appendix*, section 14. Transmission image stacks (54) were processed using a home-written MATLAB program (*SI Appendix*, section 15). The raw data and image processing codes required to reproduce the OD trajectories are available to download from https://lib.colostate.edu/find/csu-digital-repository/.

Modeling $\Delta OD(t)_d$ Trajectories. *SI Appendix*, section 16 describes the electrochemical model to determine the optically active and inactive surface charge as well as detailed fitting procedures. Briefly, $\Delta OD(t)_d$ is proportional to the time-dependent concentration of (Li-W^{5+}) color centers, $\Delta c(t)$, according to ref. 55:

$$\Delta OD(t)_d = \Delta c(t)\varepsilon_{940}/d, \quad [2]$$

where ε_{940} is the molar absorption coefficient of WO_3 at 940 nm (1×10^6 cm^2/mol) (45). For these h-WO_3 NR/ITO electrodes, $\Delta c(t)$ is equal to the

sum of the integrated Li-ion fluxes into optically active surface (J_{surf}^{active}) and bulk (J_{bulk}) sites and is given by refs. 36 and 56.

$$\Delta c(t) = \int_{t_{wait}}^{t} J_{surf}^{active}(t)dt + \int_{0}^{t} J_{bulk}(t)dt + \\ = H(t - t_{wait})\left(-\frac{A}{k_{surf}}[\exp(-k_{surf}t) - \exp(-k_{surf}t_{wait})]\right) + 2D\sqrt{t}, \quad [3]$$

where A is the amplitude of the pseudocapacative Li-ion flux, k_{surf} is the rate constant for the surface charge-transfer reaction, Q_{max} is the total charge transferred during the bulk Li-ion intercalation reaction, and the fitting parameter, $D' = Q_{max}\sqrt{D_{Li+}}/d\sqrt{\pi}$, where D_{Li+} is the Li-ion diffusion coefficient in WO_3. We assume that D_{Li+} is independent of the Li-ion insertion content (36). $H(t - t_{wait})$ is the Heaviside function that switches on the fast pseudocapacitive coloration term to fit the OD burst feature that onsets at t_{wait}.

ACKNOWLEDGMENTS. We acknowledge Zach Nilsson from Colorado State University (CSU) for electron microscopy measurements and Profs. Frank Marrs, Jean Opsomer, Mary Meyer, and Julia Sharp (CSU) for data analysis. A.E. acknowledges support from NSF and the American Statistical Association (Grant DMS-1560332). R.C.E., C.J.C., and J.B.S. acknowledge generous support from CSU. This material is based upon the work supported by the Air Force Office of Scientific Research under award number FA9550-17-1-0255.

1. N. L. Sbar, L. Podbelski, H. M. Yang, B. Pease, Electrochromic dynamic windows for office buildings. *Int. J. Sustain. Built. Environ.* **1**, 125–139 (2012).
2. N. DeForest *et al*., United States energy and CO_2 savings potential from deployment of near-infrared electrochromic window glazings. *Build. Environ.* **89**, 107–117 (2015).
3. C. G. Granqvist *et al*., Electrochromic materials and devices for energy efficiency and human comfort in buildings: A critical review. *Electrochim. Acta* **259**, 1170–1182 (2018).
4. G. Cai, J. Wang, P. S. Lee, Next-generation multifunctional electrochromic devices. *Acc. Chem. Res.* **49**, 1469–1476 (2016).
5. C. G. Granqvist, Electrochromic tungsten oxide films: Review of progress 1993–1998. *Sol. Energy Mater. Sol. Cells* **60**, 201–262 (2000).
6. S. K. Deb, Opportunities and challenges in science and technology of WO_3 for electrochromic and related applications. *Sol. Energy Mater. Sol. Cells* **92**, 245–258 (2008).
7. A. Georg, A. Georg, W. Graf, V. Wittwer, Switchable windows with tungsten oxide. *Vacuum* **82**, 730–735 (2008).
8. P. M. S. Monk, Charge movement through electrochromic thin-film tungsten trioxide. *Crit. Rev. Solid State Mater. Sci.* **24**, 193–226 (1999).
9. R. J. Mortimer, Electrochromic materials. *Annu. Rev. Mater. Res.* **41**, 241–268 (2011).
10. Z. Xie *et al*., Integrated smart electrochromic windows for energy saving and storage applications. *Chem. Commun. (Camb.)* **50**, 608–610 (2014).
11. Sage Glass, Sage Glass FAQs. (2018) https://www.sageglass.com/en/faqs. Accessed 15 February 2019.
12. E. S. Lee *et al*., "A design guide for early-market electrochromic windows" in *PIER Final Project Report* (Lawrence Berkeley National Laboratory, Berkeley, CA, 2006).
13. A. Llordés, G. Garcia, J. Gazquez, D. J. Milliron, Tunable near-infrared and visible-light transmittance in nanocrystal-in-glass composites. *Nature* **500**, 323–326 (2013).
14. E. L. Runnerstrom, A. Llordés, S. D. Lounis, D. J. Milliron, Nanostructured electrochromic smart windows: Traditional materials and NIR-selective plasmonic nanocrystals. *Chem. Commun. (Camb.)* **50**, 10555–10572 (2014).
15. M. Okubo *et al*., Nanosize effect on high-rate Li-ion intercalation in $LiCoO_2$ electrode. *J. Am. Chem. Soc.* **129**, 7444–7452 (2007).
16. V. Augustyn, P. Simon, B. Dunn, Pseudocapacitive oxide materials for high-rate electrochemical energy storage. *Energy Environ. Sci.* **7**, 1597–1614 (2014).
17. P. Yang *et al*., Quantitative analysis of charge storage process of tungsten oxide that combines pseudocapacitive and electrochromic properties. *J. Phys. Chem. C* **119**, 16483–16489 (2015).
18. P. Yang *et al*., Large-scale fabrication of pseudocapacitive glass windows that combine electrochromism and energy storage. *Angew. Chem. Int. Ed. Engl.* **53**, 11935–11939 (2014).
19. K. Wang, H. Wu, Y. Meng, Y. Zhang, Z. Wei, Integrated energy storage and electrochromic function in one flexible device: An energy storage smart window. *Energy Environ. Sci.* **5**, 8384–8389 (2012).
20. L. V. Kondrachova, R. A. May, C. W. Cone, D. A. Vanden Bout, K. J. Stevenson, Evaluation of lithium ion insertion reactivity via electrochromic diffraction-based imaging. *Langmuir* **25**, 2508–2518 (2009).
21. T. M. McEvoy, K. J. Stevenson, Spatially resolved imaging of inhomogeneous charge transfer behavior in polymorphous molybdenum oxide. II. Correlation of localized coloration/insertion properties using spectroelectrochemical microscopy. *Langmuir* **21**, 3529–3538 (2005).
22. T. M. McEvoy, K. J. Stevenson, Spatially resolved measurement of inhomogeneous electrocoloration/insertion in polycrystalline molybdenum oxide thin films via chronoabsorptometric imaging. *J. Am. Chem. Soc.* **125**, 8438–8439 (2003).
23. K. Qi *et al*., Real-time observation of deep lithiation of tungsten oxide nanowires by in situ electron microscopy. *Angew. Chem. Int. Ed. Engl.* **54**, 15222–15225 (2015).
24. P. Nachimuthu *et al*., Electronic and structural properties of 'smart windows' and liquids using in-situ X-ray absorption spectroscopy. *J. Alloys Compd.* **362**, 124–132 (2004).
25. Y.-R. Lu *et al*., Operando X-ray spectroscopic observations of modulations of local atomic and electronic structures of color switching smart film. *Phys. Chem. Chem. Phys.* **19**, 14224–14229 (2017).
26. R. C. T. Slade, B. C. West, G. P. Hall, Chemical and electrochemical mixed alkali metal insertion chemistry of the hexagonal tungsten trioxide framework. *Solid State Ion.* **32-33**, 154–161 (1989).
27. M. Hibino, W. Han, T. Kudo, Electrochemical lithium intercalation into a hexagonal WO3 framework and its structural change. *Solid State Ion.* **135**, 61–69 (2000).
28. S. Balaji, Y. Djaoued, A.-S. Albert, R. Z. Ferguson, R. Brüning, Hexagonal tungsten oxide based electrochromic devices: Spectroscopic evidence for the Li ion occupancy of four-coordinated square windows. *Chem. Mater.* **21**, 1381–1389 (2009).
29. Y. Lee, T. Lee, W. Jang, A. Soon, Unraveling the intercalation chemistry of hexagonal tungsten bronze and its optical responses. *Chem. Mater.* **28**, 4528–4535 (2016).
30. J. Wang, J. Polleux, J. Lim, B. Dunn, Pseudocapacitive contributions to electrochemical energy storage in TiO_2 (Anatase) nanoparticles. *J. Phys. Chem. C* **111**, 14925–14931 (2007).
31. V. Augustyn *et al*., High-rate electrochemical energy storage through Li^+ intercalation pseudocapacitance. *Nat. Mater.* **12**, 518–522 (2013).
32. M. Zhu, W. Meng, Y. Huang, Y. Huang, C. Zhi, Proton-insertion-enhanced pseudocapacitance based on the assembly structure of tungsten oxide. *ACS Appl. Mater. Interfaces* **6**, 18901–18910 (2014).
33. C. Jo, I. Hwang, J. Lee, C. W. Lee, S. Yoon, Investigation of pseudocapacitive charge-storage behavior in highly conductive ordered mesoporous tungsten oxide electrodes. *J. Phys. Chem. C* **115**, 11880–11886 (2011).
34. S. Cong, Y. Tian, Q. Li, Z. Zhao, F. Geng, Single-crystalline tungsten oxide quantum dots for fast pseudocapacitor and electrochromic applications. *Adv. Mater.* **26**, 4260–4267 (2014).
35. R. Giannuzzi *et al*., From capacitance-controlled to diffusion-controlled electrochromism in one-dimensional shape-tailored tungsten oxide nanocrystals. *Nano Energy* **41**, 634–645 (2017).
36. B. Vuillemin, O. Bohnke, Kinetics study and modelling of the electrochromic phenomenon in amorphous tungsten trioxide thin films in acid and lithium electrolytes. *Solid State Ion.* **68**, 257–267 (1994).
37. J. Wang, E. Khoo, P. S. Lee, J. Ma, Synthesis, assembly, and electrochromic properties of uniform crystalline WO_3 nanorods. *J. Phys. Chem. C* **112**, 14306–14312 (2008).
38. B. Miao *et al*., Large scale hydrothermal synthesis of monodisperse hexagonal WO_3 nanowire and the growth mechanism. *Mater. Lett.* **147**, 12–15 (2015).
39. J. J. Martin, A. F. Armington, Effect of growth rate on quartz defects. *J. Cryst. Growth* **62**, 203–206 (1983).
40. X. Zhou *et al*., Quantitative super-resolution imaging uncovers reactivity patterns on single nanocatalysts. *Nat. Nanotechnol.* **7**, 237–241 (2012).
41. J. Bisquert, G. Garcia-Belmonte, F. Fabregat-Santiago, Modelling the electric potential distribution in the dark in nanoporous semiconductor electrodes. *J. Solid State Electrochem.* **3**, 337–347 (1999).
42. H. J. Lewerenz, A. Heller, F. J. DiSalvo, Relationship between surface morphology and solar conversion efficiency of tungsten diselenide photoanodes. *J. Am. Chem. Soc.* **102**, 1877–1880 (1980).
43. W. Sun *et al*., High surface area tunnels in hexagonal WO_3. *Nano Lett.* **15**, 4834–4838 (2015).
44. G. A. Niklasson, L. Berggren, A.-L. Larsson, Electrochromic tungsten oxide: The role of defects. *Sol. Energy Mater. Sol. Cells* **84**, 315–328 (2004).
45. K. H. Cheng, A. J. Jacobson, M. S. Whittingham, Hexagonal tungsten trioxide and its intercalation chemistry. *Solid State Ion.* **5**, 355–358 (1981).
46. R.-T. Wen, C. G. Granqvist, G. A. Niklasson, Eliminating degradation and uncovering ion-trapping dynamics in electrochromic WO_3 thin films. *Nat. Mater.* **14**, 996–1001 (2015).
47. C. Lian *et al*., Preparation of hexagonal ultrathin WO_3 nano-ribbons and their electrochemical performance as an anode material in lithium ion batteries. *Nano Res.* **9**, 435–441 (2016).
48. D. Dong *et al*., Lithium trapping as a degradation mechanism of the electrochromic properties of all-solid-state WO_3//NiO devices. *J. Mater. Chem. C* **6**, 9875–9889 (2018).
49. C. G. Granqvist, "Devices with solid inorganic electrolytes and ion conductors" in *Handbook of Inorganic Electrochromic Materials*, C. G. Granqvist, Ed. (Elsevier Science B.V., Amsterdam, The Netherlands, 1995), chap. 29, pp. 473–488.
50. Z. Y. Liu *et al*., Characterization of carbon corrosion-induced structural damage of PEM fuel cell cathode electrodes caused by local fuel starvation. *J. Electrochem. Soc.* **155**, B979–B984 (2008).
51. D. Manka, E. Ivers-Tiffée, Electro-optical measurements of lithium intercalation/de-intercalation at graphite anode surfaces. *Electrochim. Acta* **186**, 642–653 (2015).
52. Y. Luo, W.-B. Cai, X.-k. Xing, D. A. Scherson, In situ, time-resolved Raman spectromicrotopography of an operating lithium-ion battery. *Electrochem. Solid State Lett.* **7**, E1–E5 (2004).
53. A. J. J. Jebaraj, D. A. Scherson, Microparticle electrodes and single particle microbatteries: Electrochemical and in situ microRaman spectroscopic studies. *Acc. Chem. Res.* **46**, 1192–1205 (2013).
54. J. B. Sambur, *et al*. (2019) Data associated with the manuscript: Influence of single-nanoparticle electrochromic dynamics on the durability and speed of smart windows. Mountain Scholar. https://hdl.handle.net/10217/195014. Deposited 16 May 2019.
55. J. Scarminio, A. Urbano, B. Gardes, The Beer-Lambert law for electrochromic tungsten oxide thin films. *Mater. Chem. Phys.* **61**, 143–146 (1999).
56. R. S. Crandall, B. W. Faughnan, Dynamics of coloration of amorphous electrochromic films of WO_3 at low voltages. *Appl. Phys. Lett.* **28**, 95–97 (1976).